

# The EU HeliNOVI Project - Wind Tunnel Investigations for Noise and Vibration Reduction

by  
H.-J. Langer, O. Dieterich, S. Oerlemans, O. Schneider, B. v.d. Wall, J. Yin

## Abstract

HeliNOVI was launched in April 2002 by 11 EU partners (EC, ECD, QinetiQ, SENER, VIBRATEC, CIRA, DLR, NLR, ONERA, NTUA, UMIST) with the objective to investigate the potential to reduce helicopter noise and vibration by means of configuration variations. The project was split into two main work packages: Noise reduction and vibration reduction. A third work package was defined in order to harmonize the wind tunnel test plan between noise and vibration. Project co-ordination is done by DLR.

In order to realize the demanding objectives, a Ma-scaled wind tunnel model was used which is - as much as possible - similar to a full scale helicopter allowing measurements from main rotor, tail rotor, and fuselage.

The main emphasis of the project was to create a reliable database allowing to validate theory and codes. Thus, much effort was spent to get comprehensive information about the flow conditions around the model by means of pressure measurements and PIV<sup>1</sup>.

Acoustics are measured using 16 microphones on a traverse (fig. 1). An acoustic array - located outside the wind tunnel flow - measured the rotor-generated noise pressure. In addition, high resolution pressure sensors are used, located on main rotor, tail rotor, and fuselage. In order to analyze vibration phenomena in more detail, an optical method - called SPR<sup>2</sup> - was applied. This allows to identify the local blade section position with respect to the rotor hub center. Noise reflections are suppressed by extensive usage of acoustic treatment within the wind tunnel.

Derived from flight tests, a wind tunnel test plan was established which mainly aimed to model trim conditions where acoustics or vibrations play a significant role. Although the 8m by 6m *open* wind tunnel test section was used, wall corrections were necessary and were applied.

The knowledge and understanding of important main rotor aeroacoustic mechanisms have substantially been improved over the last two decades. Validated numerical simulation codes have been developed for the most annoying impulsive noise sources like High Speed (HS) noise and Blade-Vortex Interaction (BVI) noise, while codes for prediction of the next significant broad band noise source resulting from Blade-Wake Interaction (BWI) are under development. Based on this improved knowledge, main rotor noise reductions at the order of 6 dB have been demonstrated either by active blade root pitch control (HHC, IBC) or by aeroacoustically optimised blade design.



Figure 1: Bo-105 helicopter wind tunnel model, acoustic array, and microphone traverse in the DNW 8m by 6m open test section

## 1. Introduction

<sup>1</sup> Particle Image Velocimetry

<sup>2</sup> Stereo Pattern Recognition

In contrast to the main rotor, the knowledge on tail rotor noise generating and radiating mechanisms is still in a very rudimentary state although the conventional tail rotor constitutes

an important source of helicopter noise in certain flight conditions. Especially in steep climb and at high speed level flight condition, the tail rotor represents the dominating source of annoyance of an overflying rotorcraft. In view of the expected stringency of the **ICAO noise certification rules** (envisioned reduction of 7 to 8 EPNdB) further efforts to minimise noise are essential.

Preliminary tail rotor noise investigations have indicated that the tail rotor represents an autonomous noise source with a radiation characteristic depending on the sense of rotation and in addition constitutes a source of interaction noise caused by its operation in the vortical wake of the main rotor and the main rotor hub. According to the strong perturbation of the tail rotor inflow by the main rotor wake and due to the high rotational speed, the tail rotor radiates noise at high harmonic frequency content, which strongly contributes to the annoyance of helicopter noise heard on the ground and which is very difficult to predict. To offer European industry more accurate low-noise design tools and to enhance public acceptance of future helicopter operation in densely populated areas, within the proposed project the (tail) rotor noise prediction and noise reduction capability will be improved.

In contrast to external noise radiation which is characterised by "high frequency" aerodynamic effects in the kiloHertz range, helicopter vibration phenomena are related to both aerodynamic excitation and structural dynamic characteristics of rotor and airframe in the low frequency domain up to about 200 Hz. For the isolated rotor, the dynamic and aerodynamic characteristics are well understood leading to design guidelines for favourable low vibrational behaviour (e.g. de-tuning of the rotor blades). Today, the main difficulties in vibration prediction consists in the determination of the excitation sources affected by wake and interactional effects. The existence of an airframe in the vicinity of the rotor results in flow displacement and lifting body effects modifying significantly the aerodynamic environment. This interactional aerodynamic phenomenon is two-sided: The downwash of the rotor changes the airframe flow field, resulting in a coupled problem of rotor – airframe interference. The modified local angles of attack acting on the rotor blade sections have a direct impact on the airloads and response of the rotor and thus, on overall helicopter vibrations.

Due to code and computational power limitations, the theoretical investigation of interactional effects has started, in the past, with investigations concentrating on time

averaged aerodynamic interference effects which have been extended in the meantime substantially covering unsteady aerodynamic interference. Nowadays, the progress of the related software tools allows the integration of rotor dynamics in the calculations and the investigation of interactional effects on vibratory hub loads. Nevertheless, due to limited available data, additional effort has to be spent for the validation process of these tools for successful application in industry. For this purpose, wind tunnel tests of a Mach scaled helicopter model was performed. This scaling of the wind tunnel model offers the opportunity to combine the test results with flight measurement data of the full-scale rotorcraft for a unique database in Europe. Variations (e.g. rotor hub distance, tail rotor location) of the wind tunnel model configurations were tested and used for validation of the prediction design tools and evaluation of vibration reduction means. The improved design tools will support the engineer to consider interactional aerodynamic effects already during the design phase for low vibration helicopters shortening time to market.

## 2. Wind Tunnel Model

### 2.1 General

The wind tunnel model is based on the so-called MWM (Modular Wind Tunnel Model) [1] which represents the core system of the model. It consists of the drive system (135kW hydraulic motor at 1050rpm), the 6-component rotor balance, the swashplate control system (3 boosters), and the data amplification unit in the rotating system. For the wind tunnel tests the Mach-scaled Bo105 rotor (R=2m) was used.

Besides the main module additional components were installed:

- fuselage shell
- fuselage balance
- hydraulic drive motor for tail rotor
- tail fin integrated tail rotor
- sensors

Technical data of the main rotor and tail rotor are listed in Table 1.

The 6-component *fuselage balance* is of integral type. It measures the total forces and moments acting on the fuselage with respect to ground i.e. is totally separated from the *rotor balance* system. The balance forces and moments include the tail rotor loads and the torque from the tail rotor drive system.

For the hydraulic hoses swivel joints are used in order to avoid load crosstalk on the fuselage balance (Fig.2).

Property	MR	TR
no. of blades	4	2
rotor type	hingeless	teetering
radius	2 m	0,383 m
radius scale factor	2.455	2.48
chord	0.121 m	0.074 m
root cut-out	0.44 m	0.16 m
solidity	0.077	0.123
precone	2.5°	0°
pretwist	-8°/R	0°/R
pitch-flap coupling	0°	45°
tip Mach number (ISA)	0.64	0.65
lock number	8	4.2
shaft tilt forward	3°	-4°
shaft tilt upward	0°	-3°
airfoil	NACA 23012	S102E

Table 1: Main Rotor (MR) and Tail Rotor (TR) Data

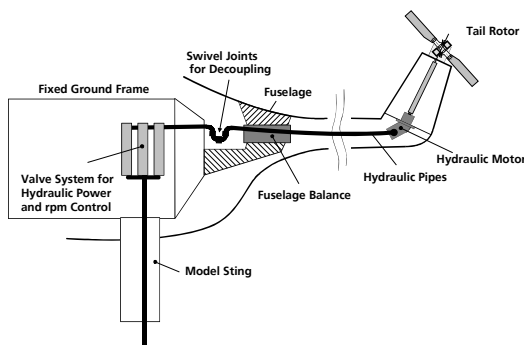


Figure 2: Tail Rotor Drive System

## 2.2 Sensors & Instrumentation

Due to the high number of sensors, most of preparation time outside the wind tunnel was consumed to install and calibrate sensors.

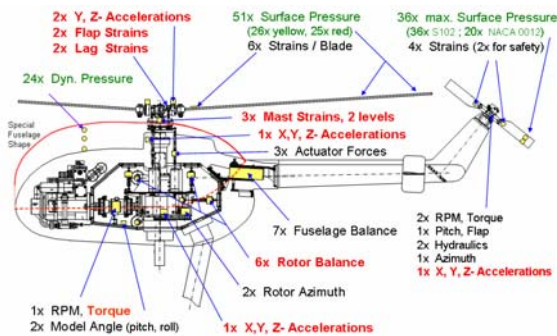


Figure 3: Model Sensors and Location

In order to allow a precise and all-encompassing evaluation of wind tunnel experiments, the model is instrumented with a large number of individual sensors (e.g. pressure transducers, strain gauges) and composed sensors (e.g. balances, accelerometers, etc.). Most of the individual sensors are distributed on the rotor blades (main rotor and tail rotor), i.e. rotating frame, whereas the composed sensors are all in the fixed frame.

The location of most sensors is shown in *fig 3*.

While the main rotor thrust is measured via the 6-component rotor balance, the tail rotor thrust was derived using the 0/rev blade bending of a tail rotor blade. Since the thrust correlates quite well with coning, at least up to  $\mu = 0.2$ , the blade root bending moment – measured with a strain gauge - is a good measure to determine the thrust. The calibration of the tail rotor was made during hover tests at 5525rpm using the fuselage balance as reference. This allows to eliminate centrifugal effects from the calibration curve.

TR 1/rev flapping is important for code validation and trim, therefore a Hall sensor was used that enabled the measurement of the flap movement of the gimbaled tail rotor hub. Although the calibration curve is non-linear, online data processing allows exact display of the 1/rev amplitude for safety reasons.

## 2.3 Rotor Balance Dynamic Calibration

Although not designed for dynamic data analysis, the rotor balance was analysed with respect to dynamic calibration at 4/rev - i.e. at 70Hz. Different configurations were investigated and special emphasis was given to find out possible differences between calibration with dummy blades i.e. equivalent blade masses and normal blades. In order to be as close as possible to the reality, the calibration was made with rotating rotor hub (*Fig.4*).

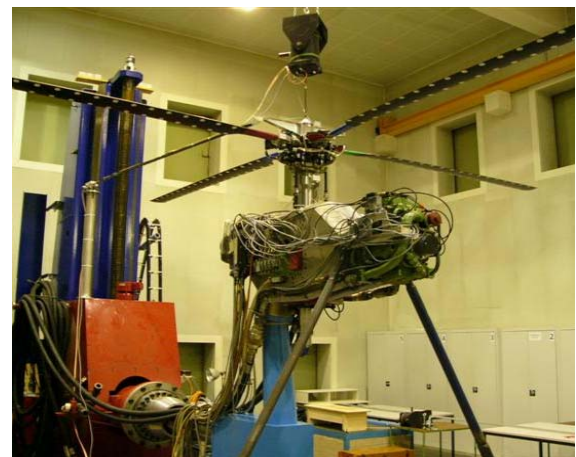


Figure 4: Test set-up for rotor balance dynamic calibration

For a helicopter with a 4-bladed rotor the amplitude of 4/rev vertical vibration is of most interest. Therefore an example is given showing calibration results in z-direction i.e. thrust direction.

Since the Z-force transducers of the rotor balance have the strongest part for 4/rev  $F_z$ , *Fig.5* gives an impression of the difference between calibration with blades and with blade

dummy masses - both at nominal rotor revolution ( $\approx 1050\text{rpm}$ ). Due to a non-symmetric arrangement of the balance, the Z2-Piezo sensor is higher loaded which is confirmed by both calibration methods. Analysing the difference between both cases for Z2 it should be kept in mind that in case of the calibration with blades, dynamic and aerodynamic loads have to be considered while for the case of dummy loads only inertia loads appear. Furthermore, a slight overweight set-up exist with respect to the dummy mass configuration regarding theoretically obtained modal masses,

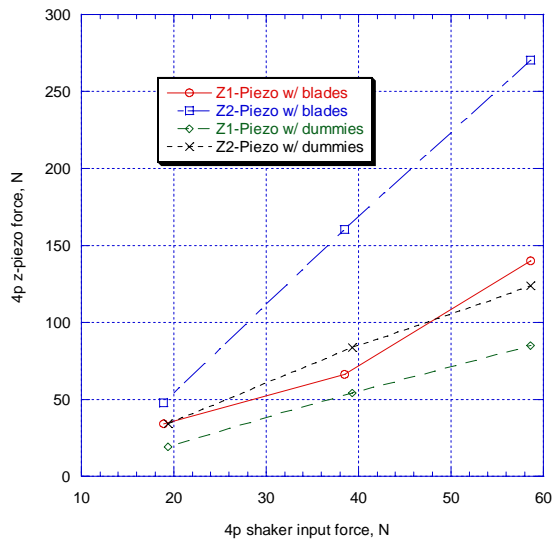


Figure 5: Dyn. Calibration with 4/rev shaker force @ 1050rpm in z-direction

Concerning the  $F_z$  rotor mast sensor the correlation is better because the differences are small between both calibration methods (Fig.6).

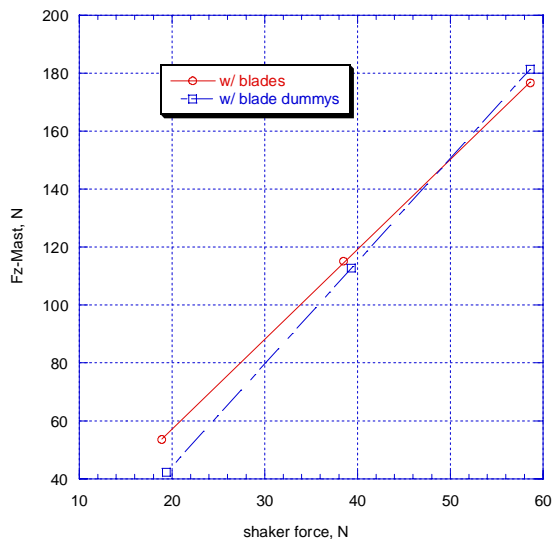


Figure 6: Dyn. Calibration for 4/rev Mast Force in z-direction

Generally, the dynamic calibration of the rotor balance showed a very high sensitivity for 4/rev vibration analysis in thrust direction making the direct application of the calibration results difficult. This is mainly due to a rotor balance resonance frequency which is close to the 4/rev rotor frequency. Thus, the model support has a strong impact on calibration results. In any case, it is recommended to accomplish such tests "with blades" - and not with blade dummy masses - on a model support where the final test takes place: on the DNW sting support (Fig.1). Future activities will show whether the consideration of accelerometer signals will improve the situation.

### 3. Wind Tunnel Tests

The total tunnel occupation time was fixed to 120 hours. This included

- build-up and removal of helicopter model
- background noise investigations
- installation and removal of
  - microphone traverse
  - acoustic array
- removal of acoustic floor coating
- preparations for dynamic balance calibration
- PIV setup and removal
- SPR setup and removal
- all model related configuration changes (see section "Model Preparation")
- priority test points from the test matrix

Due to the high number of configurations which have to be tested, most of the tunnel occupation time was spent on configuration changes.

#### 3.1 Data Processing

Fig. 26 (see appendix) shows details of the rather complex data acquisition, - processing and - distribution system. Three data recording units are available for

- basic data
- acoustic data
- dyn. pressure data

Not listed are the DNW acquisition systems for PIV, microphones, SPR, and the NLR operated acoustic array.

### 3.2 Configurations

#### 3.2.1. Test Section Equipment

For the noise wind tunnel test programme the wind tunnel test section is equipped with a microphone traverse holding 16 inflow microphones. Three microphones were positioned out-of-flow as well as the acoustic array where a bunch of microphones are placed.

The array<sup>3</sup> consists of 140 microphones which locate and quantify noise sources, i.e.:

- to distinguish between MR noise from TR noise
- identify sources in rotor plane (e.g. BVI noise)
- identify sources on rotating blades

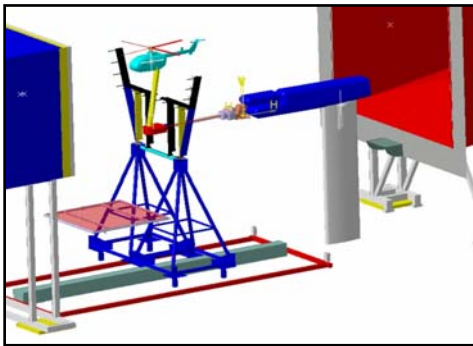


Figure 8: Acoustic array (red) and traverse with inflow microphones (black); (courtesy DNW)

Since the array is fixed to the mic-traverse, measurements are taken upstream and below the model (Fig. 1, Fig. 8).

Data of array microphones is synchronous with inflow microphones and blade pressures.

For data acquisition 20 seconds are used at fixed sample frequency of 51.2 kHz. W.r.t. the total data acquisition time for one data point, almost no extra time is needed to take and store data.

Results are used for fast comparison of different configurations (e.g. flight conditions), are complementary with inflow 'footprints', and allow correlation with blade pressures. An exemplary result is shown in Fig. 7. Well visible is, that the source location is clearly dependent on the flight condition.

After removal of the microphone traverse and acoustic floor treatment, PIV test set-up was installed (Fig. 9, Fig. 27).

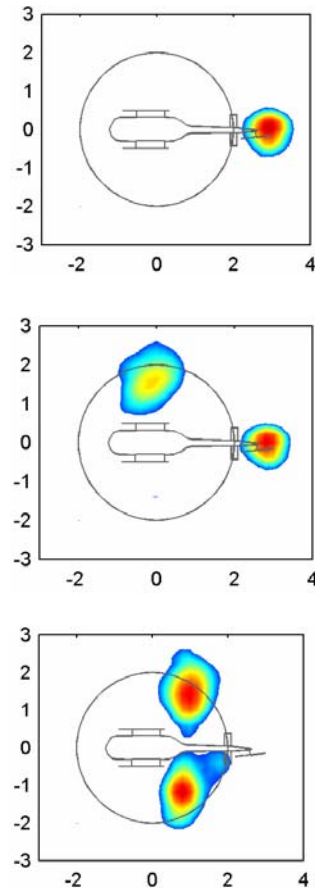


Figure 7: Mic. array pressures for MR+TR at 1600 Hz for climb(top), level(middle), and descent(down)

#### Stereo PIV measurement set-up

In order to cover the proposed test matrix of measurement locations, a common support was used that had three traverses (7.6m in x, 2.1m in y, and 1.7m in z direction) plus a central hinge for rotations about the vertical axis, see Fig. 27.

On the lower platform two double-pulse lasers were mounted, their beams were directed vertically into the flow and aligned on the same plane with a thickness of 7mm for maximum light energy. The camera systems were mounted on the z-traverse of the common support's vertical tower such that the entire main rotor and tail rotor area could be measured.

<sup>3</sup> Operation, data acquisition, and data analysis by NLR

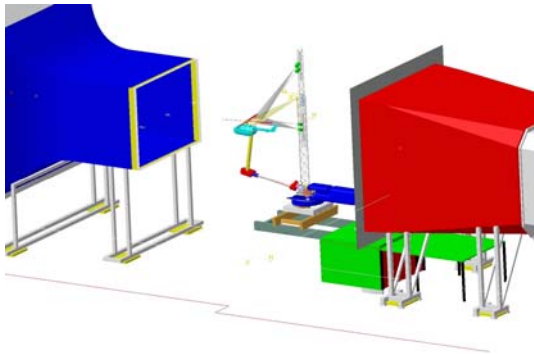


Figure 9: PIV Test set-up principle (courtesy DNW)

For measurements on the other side of the main rotor, the entire common support was moved to the other side of the model.

In this setup, the vertical distance between the cameras was 7.1m and the horizontal distance to the light sheet could be kept constant to 5.7m during all PIV measurements. Therefore, a pixel-to-length re-calibration and camera alignment (which usually has to be performed after each change in the setup) could be avoided.

Atomized particles were pumped through a distribution rake mounted in the settling chamber of the wind tunnel. The rake was remotely traversed to guide the homogeneous seed stream to the region of interest. The droplets generated and distributed by this arrangement have a mean diameter below  $1\mu\text{m}$  as confirmed by previous tests. Inside the tip vortex the seeding density is noticeably lower than in the remainder of the flow field. This can be explained by the reduced air density inside the core and centrifugal forces that effect the particle distribution. The CCD cameras (1280x1024 pixel resolution, 12bit grey scale) had 135mm lenses and were spaced vertically such that one camera was looking from below the observation area, and the other camera from above.

For measurements in the main rotor area the trigger to the rotor azimuth was varied from 0deg to 78.75deg in increments of 11.25deg. At each of these reference azimuths six data sets were taken from different blades.

The measurement plane was parallel to the flow and the observation area was traversed from the front to the rear of the rotor disk, extending up to 4m.

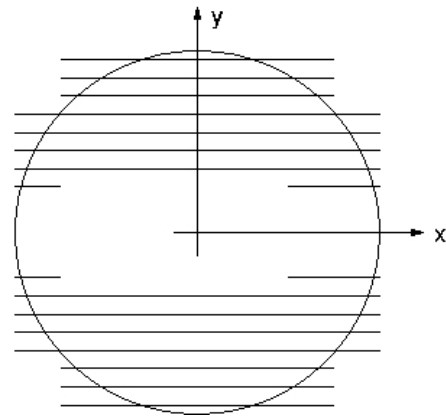


Figure 10: PIV traversing locations below the main rotor disk for vibration measurements

Nearly the entire main rotor disk was covered by additionally traversing in lateral direction from  $y/R = 0.25$  to 0.95 in increments of 0.1 (Fig.10), and by placing the common support to the other side of the model. The main purpose was to measure the inflow velocities in the main rotor tip path plane and the main rotor wake geometry.

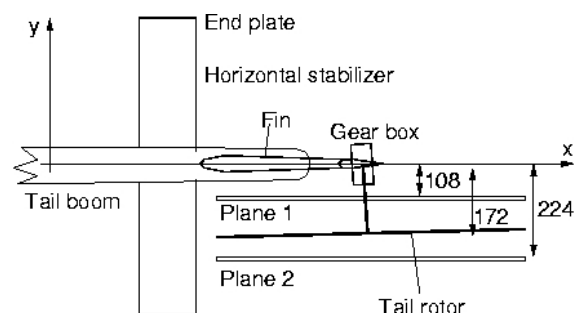


Figure 11: PIV measurement planes in the tail rotor area

For tail rotor measurements, one measurement plane was located on the suction side of the tail rotor 108mm away from the disk and the second plane was located on the blowing side 52mm away from the disk (Fig.11). The trigger was made to the main rotor azimuth from 0deg to 150deg in increments of 30deg. Thus, the main rotor tip vortex flight path through the tail rotor disk was covered.

Five positions of the observation area with some overlap were selected to cover the entire tail rotor area, except where the horizontal stabilizer and its end plates prohibited any measurements. The observation area covered 378mm horizontally (almost the tail rotor radius of 383mm) and 339mm vertically. The purpose was to measure the tail rotor inflow and outflow, and to identify effects of main rotor/tail rotor interactions.

### Flow field analysis

The raw data analysis, i.e. computation of velocity vectors from the camera images, was performed by DNW. As a result, 48 individual flow field data sets were available per position for the main rotor measurements, while 200 individual flow field data sets were available per position and main rotor azimuth for the tail rotor measurements. Each data set was represented by 79 by 71 vectors with 50% overlap of the cross-correlation windows of 32x32 pixel size.

As already mentioned tail rotor and main rotor drive systems were completely independent from each other. Data acquisition was triggered to the main rotor azimuth.

In the main rotor data a rotor blade often is in the image due to the azimuth position and aside from spurious vectors caused by its presence in the observation area; it created a shadow above it such that no vectors were available upon it.

Due to the trigger to the main rotor azimuth the tail rotor blade was arbitrarily visible in the vector fields and made the analysis impossible in about a quarter of the data of the tail rotor measurements.

A simple average of all individuals provides a good overview of the flow field and the location of the main rotor tip vortex, which was cut almost orthogonal by the set-up.

For an analysis of this tip vortex a conditional average must be made, i.e. aligning all individual vortex centres first, eliminating all unuseful exposures using statistical analysis, and then averaging [9]. This eliminates the data noise but retains individual properties that got smeared out by the simple average, and also eliminates data with disturbances caused by a blade passage. A rotation into the vortex axis system was not performed, since the measurement plane was almost orthogonal to the vortex. The analysis steps are described in [10].

The resolution of a PIV measurement is defined by the length of the cross-correlation window,  $L_m$ , divided by the core radius of the vortex to be observed,  $r_c$ . Assuming 5% of the main rotor blade chord as core radius, a ratio of  $L_m/r_c = 1.6$  was present in the data. A value of 0.2 is recommended for vortex property analysis purposes like identification of core radius, maximum swirl, or circulation [11]. During the HART II test, a value of  $L_m/r_c = 0.5$  was used which was sufficient for most of the vortices measured, but still not yet enough for the youngest vortices in some cases [12]. Therefore, vortex properties analysed from the HeliNOVI PIV data have to be handled with

care. However, it must be noted that the main purpose of these measurements was to measure global flow distribution, plus the vortex flight path, and not the vortex properties.

### SPR Analysis

The measurements of the blade deflection were made by means of SPR (Stereo Pattern Recognition). With this method, the spatial position of markers painted on each of the four blades and to the fuselage is determined optically by two cameras with different locations (*Fig. 12*). The technique is based on a 3-dimensional reconstruction of visible marker locations by using stereo camera images. The accuracy of marker position recognition theoretically is about 0.4 mm in x-, y- and z-direction. A more detailed description of the method is presented in [6]

For the SPR measurements two different camera systems were used, one at the advancing side and one at the retreating side. Each camera system contains two cameras mounted on the ground of the wind tunnel hall, located in front and in the back of the model. For calibration of the SPR system special reflective marker were taped on all blades and were localized by means of Theodolites.

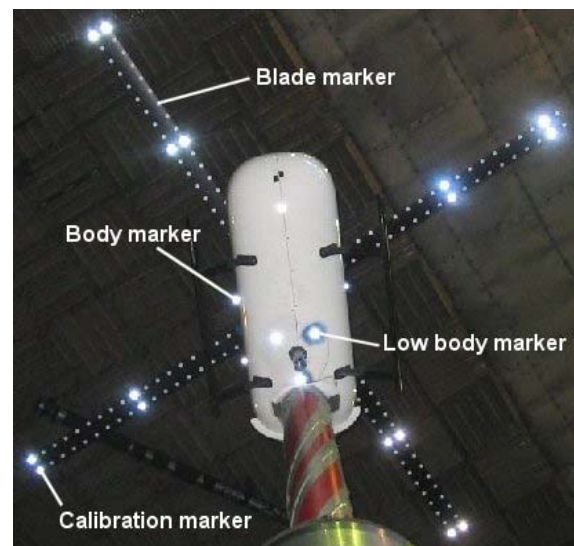


Figure 12: Marker locations for SPR measurements

For the HeliNOVI tests, a total of 36 white markers (18 at the leading edge and 18 at the trailing edge, called blade marker) were painted on each rotor blade (from 23% to 99.4% radius). Additionally, for purposes of hub center localization and drift compensation 3 markers were attached underneath the fuselage shell (lower body markers) and 2

markers on each side of the shell (body markers). Measurements were done with an azimuth increment of 11.25 deg respectively 32 azimuth positions per revolution. On each azimuth position 50 images were taken for averaging to get smooth data with reduced errors and eliminated vibrations. The blade deflection measurements contained 3 different configurations.

In pre-processing the camera images were evaluated by DNW which results in x-, y- and z-positions of blade and body markers in the wind tunnel coordinate system. To eliminate fluctuations a mean value of all 50 images is computed. Generally open sting axis (= model support) show a small drift but is corrected automatically into its nominal position. Therefore a drift correction for all coordinates is made analyzing the movement of the body markers.

### 3.2.2. Helicopter Model

The following model parameters are investigated:

- main rotor (MR); tail rotor (TR) with blade profile S102E; fuselage (orig.) as baseline tests
- MR; TR-S102E new vertical position, i.e. tail boom up by  $r_{TR}$  (see Fig. 13)
- MR 10% rpm reduction
- MR only (TR blades removed)
- TR-S102E only (MR blades removed)
- MR; TR with profile NACA0012
- TR-NACA0012 in tractor and pusher mode
- TR-NACA0012 only, MR removed
- MR; TR-NACA0012, counter-clockwise rotation
- Modified fuselage contour (vibration tests only); see Fig. 14
- rotor thrust

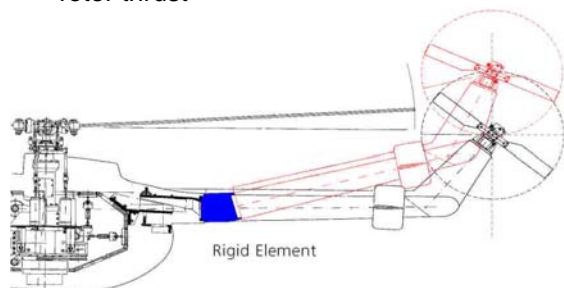


Figure 13: New tail rotor position

### 4.2 Trim Procedure

The general trim procedure aims to balance the BO 105-model weight, aerodynamic forces, and moments on the helicopter model in the

wind tunnel such that their total sum in geodetic system is zero.

In order to achieve a rapid trim condition a software commands MR and TR control angles, based on derivative or previous measurements, for a given tunnel speed and fuselage attitude angle. Although the final trim could be reached faster using automatic control, a semi-automatic procedure - leaving the pilot in the control loop - seems to be safer.

### 4. Exemplary Results

A detailed analysis of measured results goes beyond the scope of this paper, however, is presented in [2], [3], and [4].



Figure 14: Fuselage contour modification

In order to underline the helicopter model and the DNW-LLF capabilities, some exemplary results are shown (some results from Acoustic Array measurements are already shown in section "Configurations").

#### 4.1 Helicopter Model Database

The HeliNOVI test matrix contained three data points which allow a direct correlation with test runs from a previous campaign - the so-called "WiVal"<sup>4</sup>[8]. Regarding the wind tunnel model configuration, the test campaigns differ by the different main rotor blade sets and by the tail rotor system which was not available for the WiVal test campaign.

In order to check the repeatability, wind tunnel speed, thrust, rotor revolution, mast moments, and rotor shaft tilt was equally set. Fig.15 shows HeliNOVI (HN) and WiVal (WIV) results for 4/rev blade flap at 15% radius and 3/rev lead-lag at 17% radius. All sensors show the typical curve shape: Minimum vibration at very low speed and around 50m/s and higher vibration around 20m/s and at high speed.

<sup>4</sup> Aim: Data correlation between flight tests and wind tunnel tests (in co-operation with NASA/USArmy)

In general the correlation is good although the HeliNOVI and the WIVal main rotor blade sets were built by different manufacturers.

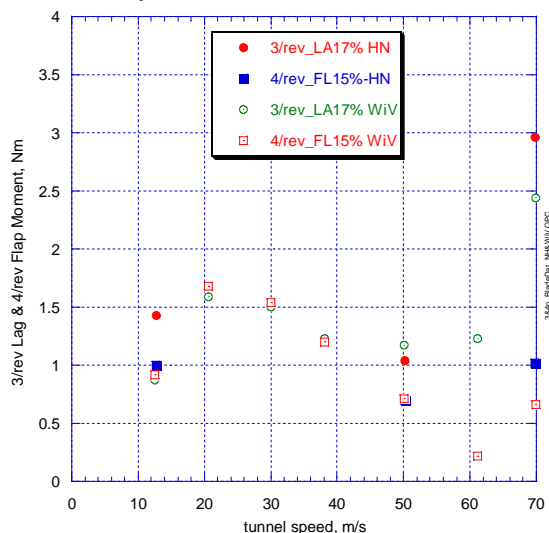


Figure 15: Repeatability check between HeliNOVI and WIVal test campaign

For data correlation with flight tests (Bo105), flight trim condition was directly applied to the HeliNOVI model. Focus was given on a similar loading situation of the main rotor and the tail rotor. This was accomplished by applying the scaled down mast moment, the overall helicopter mass, the forward speed, and the wall-corrected fuselage pitch to the wind tunnel model. The scaled down helicopter mass was compensated by the total model lift w.r.t. the location of the center of gravity of the Bo105.

Fig. 16 and Fig.17 show some correlation results concerning lead-lag moment and flap moment. The position of the sensors is at the blade root for the lead-lag moment and on the rotor hub for the flap moment.

The correlation in lead-lag is quite well for 3/rev, especially at higher speeds. For 4/rev flap moments the agreement between the measurements is similar with the exception of low speed where a certain discrepancy between flight and wind tunnel is more obvious. It looks that the transition regime (around 10m/s) is not well matched in the wind tunnel which is likely due to the applied significant global flow correction of an open wind tunnel jet. The role of wind tunnel corrections on vibratory loads is still under investigation.

The speed of minimum vibration shows a good correlation - likely due to the more accurate flow correction.

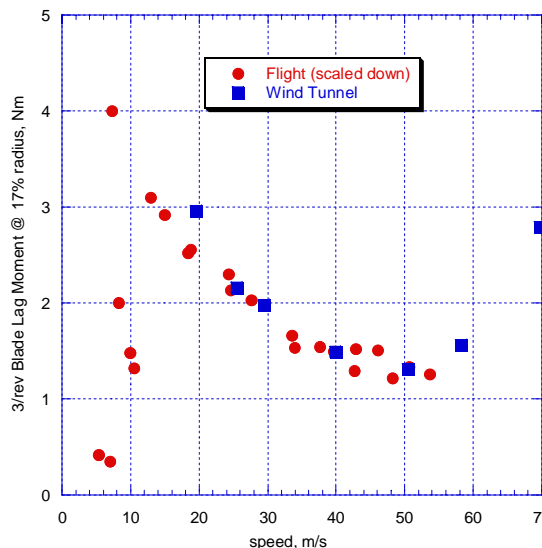


Figure 16: 3/rev lead-lag correlation between flight tests and wind tunnel tests

Beside unknown wind tunnel flow effects, flight tests have some uncertainties, too. On the one hand it is difficult to keep the helicopter in steady-state conditions at low speed (Fig. 18), on the other hand to accurately measure the forward speed depends on a high quality airspeed sensors and on wind conditions.

In any case, results from Fig. 16 and Fig. 17 show that wind tunnel measurements can well be used to determine certain aspects of the vibration characteristic of rotor or helicopter systems in flight, supposed that adequate scaling is applied to the relevant model components e.g. the main rotor blades are Mach-scaled and thus dynamically scaled.

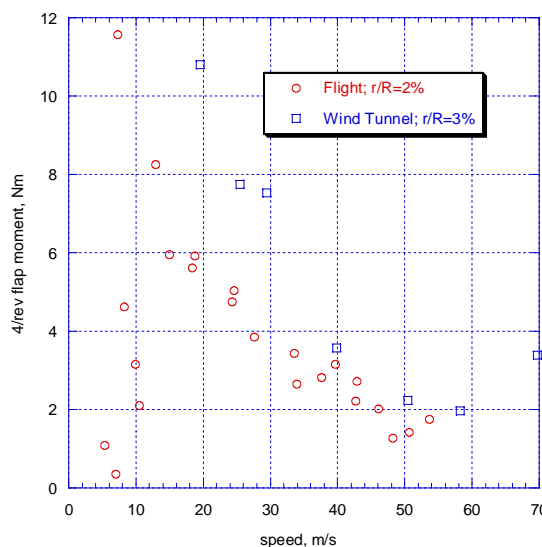


Figure 17: 4/rev flap moment correlation between flight tests (scaled down) and wind tunnel tests

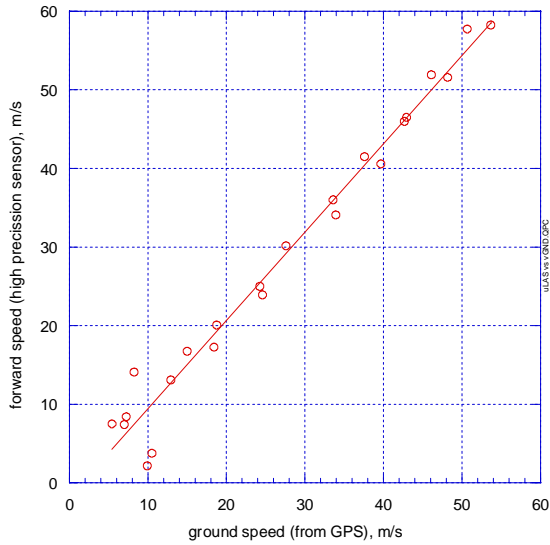


Figure 18: Scatter of forward flight speed measurement

#### 4.2 Acoustics

The acoustic results consist of acoustic time history, spectrum and footprint from inflow and output flow microphone. The tested configurations in aeroacoustic part are

1. tail rotor sense of rotation (NACA 0012 blade profile)
2. variation of position between main rotor and tail rotor (S102 blade profile),
3. variation of TR rotational speed.

The flight conditions covered level, climb and descent flight in various flight speeds.

The potential of tail rotor noise reduction is observed especially by changing tail rotor sense of rotation for 12° climb and 60m/s level flight where TR noise is dominant source of noise.

The acoustic inflow contour plots shown in Fig.19 demonstrate the influence of different TR rotation on noise radiation for 12° climb at 33m/s flight condition. The comparisons show the noise reduction at maximum noise area is about 8 dBA for the 12° climb case (Fig.19, red dot) and about 6dBA for 60m/s level flight condition when TR sense of rotation changed from Advancing Side Down (ASD) to Advancing Side UP (ASU) rotational direction. There is no change for 6° descent flight condition because the MR BVI noise is dominating. The results of noise reduction by reversing TR are in contradiction with results (Westland Lynx) from previous TR noise research. The detailed analysis on MR/TR interaction and TR noise reductions is given in [4]

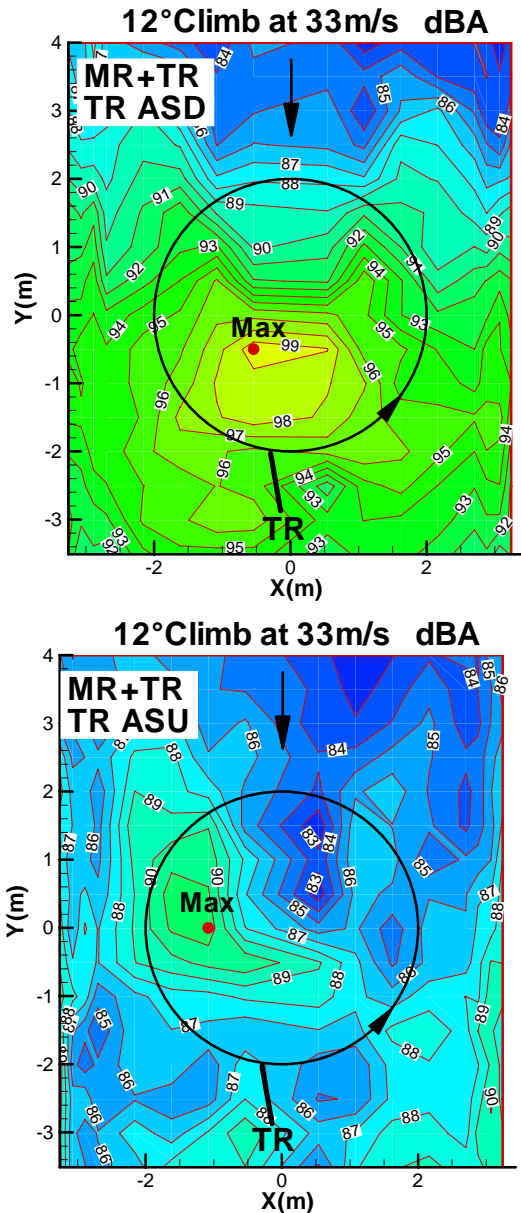


Figure 19: Effect of tail rotor sense of rotation on tail rotor noise radiation. Top: advancing side down (ASD); bottom: advancing side up (ASU)

#### 4.3 Flow Visualisation (PIV)

##### A. Main Rotor Global Flow Field

The global flow field of a low speed steep descent condition at  $v = 12\text{m/s}$  is shown in Fig.28. From the left to the third image the oncoming flow is present until the tip vortices (in red) indicate the border of the rotor slip stream. Up to here the tip vortices are close to the tip path plane, which is represented by the thick black line, and cause oblique blade-vortex interactions. From here to the right the flow is dominated by the induced velocity field directed downwards, which is visible in the convection of the shed wake (long red line) of

the blade that just passed the observation plane at the right of the figure, leaving its tip vortex clearly visible (blue area in the right image).

The main rotor tip vortex is visible at  $(x, z) = (-3, 56)$  and  $(-6, 45)$  and from the blade just leaving the plane at  $(x, z) = (102, 40)$ . Reflections from the blade leading edge indicate its position in the figure at  $(x, z) = (-36, 64)$  and the shed wake from the passing blade is the red line from the centre to the right. The cut of the rotor cone is indicated by the black line, the rotor centre is located at the “+”.

**B. Induced Velocity Field**

The mean induced velocities can be extracted from the averaged vector maps. The results are shown in Fig. 20 for all three components. The free-stream velocity of 12m/s is subtracted from the horizontal component  $V_x$ , such that all velocities represent pure induced velocities from the rotor, the fuselage, and tunnel interference. At the front of the disk the horizontal component is negative, i.e. the flow is decelerated by the presence of the rotor. At the front of the disk a small region of upwash is visible, followed by a continuously increasing downwash area.

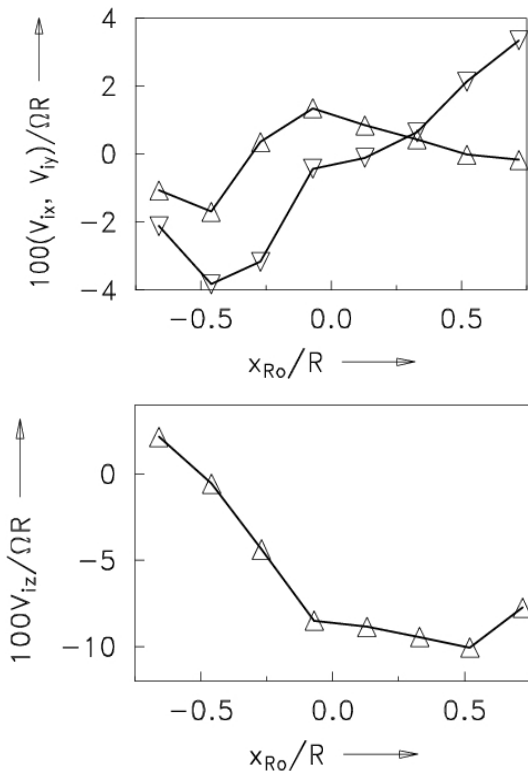


Figure 20: Top: Induced velocities horizontal ( $\Delta$ ) and lateral ( $\nabla$ ). Bottom: vertical induced velocities.  $V = 12\text{m/s}$ ,  $\alpha = 8.1^\circ$ ,  $y_{Ro}/R = -0.721$

The measurement areas are located below the rotor disk and ahead of the slipstream tube boundary, compare to Fig. 28. Downstream of

$x_{Ro}/R = -0.3$  the flow is accelerated, which is explained by the measurement area locations within the slip stream of the rotor. The lateral flow is directed outboard up to the rotor centre, then directed inboard for the rest. Much larger induced velocities are found in the vertical component.

This representation can be made for all lateral positions to form a global induced velocity distribution for comparison with numerical models. In addition, the dynamic content can be extracted from the data since each location was measured at different rotor azimuth positions.

**B. Tail rotor Global flow field**

An overview of the simple average flow field of plane 1 (between the tail rotor and the fin) and plane 2 (blowing side of the tail rotor), with the mean velocities subtracted, is given in Fig. 29. The main rotor tip vortex enters in the middle of the left side and is convected downstream and downwards to the right. Reflections from the fin are much less in plane 2 due to the larger distance. The rotor hub is located at  $(x, z) = (-41.5, 30)$  and the shaft angle of attack is  $-13.5^\circ$ , representing a  $12^\circ$  climb case.

The main rotor tip vortex is visible at  $(x, z) = (65, 56)$  for  $\Psi = 30^\circ$  and  $(90, 49)$  for  $\Psi = 120^\circ$ . Reflections from the fin indicate its position in the figure (bottom left to the centre). The tail rotor disk is indicated by the large circle.

The high speed forward flight case is shown in Fig. 30. Only three of the 5 observation areas were covered here. Again, the fin is reflecting in the middle, and in plane 1 the drag of the tail rotor shaft is dominating the right half of the figure. Reflection effects are significantly reduced in plane 2. The main rotor centre is located at  $(x, z) = (-22.4, 45)$  and the shaft angle is  $-6.6^\circ$ .

The main rotor tip vortex is visible at  $(x, z) = (93, 60)$  for  $\Psi = 30^\circ$ . Reflections from the fin indicate its position in the figure (centre). The tail rotor disk is indicated by the large circle.

**C. Vortex flight path**

The tip path plane of the main rotor is separated to that one of the tail rotor by 69mm horizontally and the main rotor hub is 27mm above the tail rotor centre. With the precone of  $2.5^\circ$ , assuming no elastic deformation relative to this precone (the elastic deformations were not measured for the flight conditions investigated here) and accounting for the

different lateral positions of the measurement planes the origin of the main rotor blade tip vortices can be estimated. These positions are taken as creation points of the blade tip vortices passing through the PIV planes.

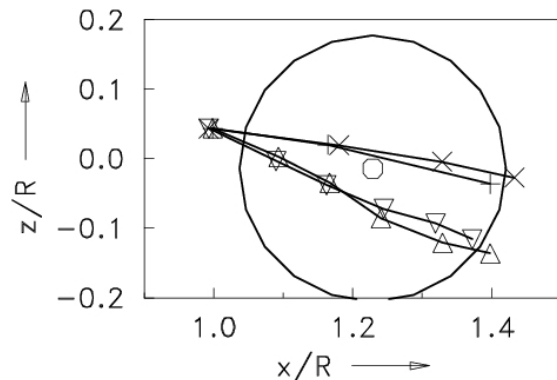


Figure 21: Main rotor vortex flight path through the tail rotor disk.  $V=33\text{m/s}$ ,  $12^\circ$  climb:  $\Delta$  (plane 1),  $\nabla$  (plane 2).  $V=60\text{m/s}$ , level flight:  $+$  (plane 1),  $\times$  (plane 2). The tail rotor disk is indicated by the large circle, its centre by the small circle.

In Fig. 21 the vortex flight path through the PIV planes is given in rotor hub coordinates. The time increment between the symbols is  $30^\circ$  of main rotor azimuth, and the rightmost position of ( $\times$ ) is a guess, it is just outside the PIV window in most of the data sets. The rightmost position of ( $+$ ) is  $90^\circ$  later than the preceding symbol. The vortex is clearly visible at  $\Psi = 30^\circ$  in both flight conditions, and also for  $\Psi = 60^\circ$  at  $v = 33\text{m/s}$ . These positions are ahead of the area affected by fin and tail rotor hub reflections.

In plane 1, the vortices of the high speed case closely pass the tail rotor hub and are difficult to detect thereafter (Fig. 30). The disturbances were not that severe in the low speed climb condition where the vortices pass below the tail rotor hub. Some differences in convection become visible after passage of the tail rotor hub. At low speed climb the convection in plane 1 ( $\Delta$ ) is larger than in plane 2 ( $\nabla$ ), which can be explained by the suction and associated acceleration on this side of the tail rotor disk. It is vice versa in high speed level flight. In this case the presence of the tail rotor shaft appears to decelerate the flow. In any case the vertical position becomes different after passage of half the tail rotor disk area.

#### 4.4 Rotor Blade Position (SPR)

For calculation of the blade deflection and blade motion parameters, the rotor hub center location must be known in order to transform the coordinates from the wind tunnel system

into the hub center system. The position of the hub center could not directly be measured. To localize the center position in the rotor plane (x-y-direction) a circular regression is used after transforming all data by shaft and roll angle (Fig. 22). More details are presented in [5]. With the assumption that each single blade marker travels along a circle around the hub center a best fit can be calculated where the center point of the circle is the center position of the rotor. Thus one gets 36 center points per blade from the 36 blade markers. The comparison of the results shows a range of less than 0.5 mm in x-y-direction where all computed center points of all four blades are within.

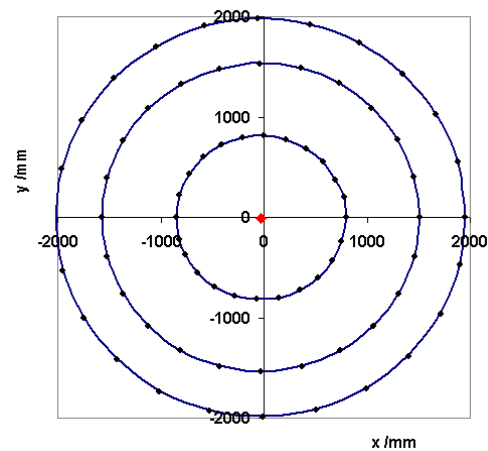


Figure 22: Best fit circles for identification of hub center

The vertical hub center location can be obtained by using the body marker. With the known geometry the hub center position can be calculated with an error of less than 0.5 mm since the marker recognition accuracy is 0.4 mm.

#### Blade motion

After transformation of all marker coordinates into the hub center system the blade motion is computed. All blade motions like flap, lead lag and torsion are related to the quarter chord line of the blade which is calculated by interpolation from the leading and trailing edge blade markers. The elastic flap deflection can be obtained by the distance of the quarter chord line to a straight line defined by the precone angle of the blade. The elastic blade lead lag deflection is given by the distance between the radial position of the quarter chord line and a straight line defined by the current azimuth position of the blade. For the calculation of the elastic blade torsion the vertical position of the leading and trailing edge blade markers is used where the controlled pitch angle and the linear blade pre-twist have to be considered.

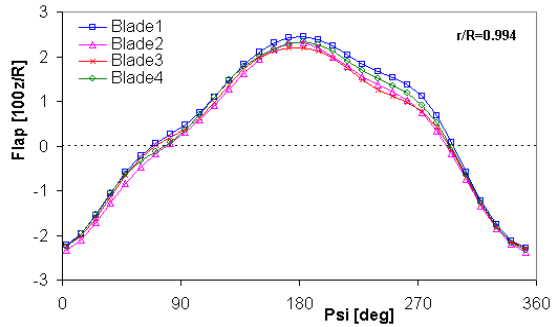


Figure 23: Elastic blade tip motion in flap, wind speed 12 m/s

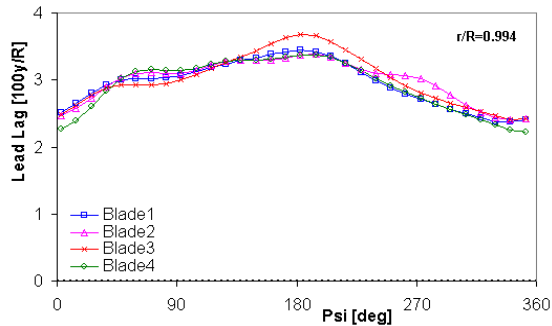


Figure 24: Elastic blade tip motion in lead-lag, wind speed 12 m/s

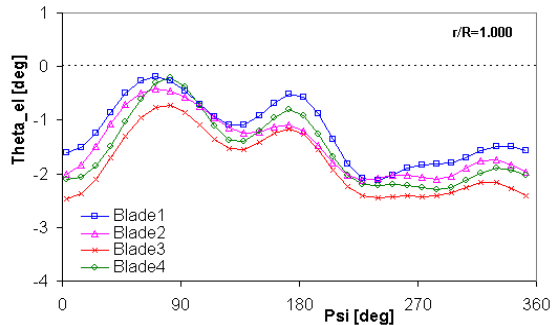


Figure 25: Elastic blade tip motion in torsion, wind speed 12 m/s

To get an analytical description of the blade motions Fourier coefficients up to 5/rev were calculated for each radial station by 'best fit' over all azimuths. For blade flap, lead-lag, and torsion results are shown in Fig. 23 to Fig. 25.

SPR data can well be used to identify differences in the dynamic behaviour of the blades. In a future step the data will be compared with strain gauge measurements.

## 5. Prospects

The wind tunnel model described in this paper will be used for future tests, where a scaled 'main rotor - tail rotor - fuselage' configuration is required.

Within the 6<sup>th</sup> European Framework Program 'GROWTH' a new project is launched in 2005 - called 'GOAHEAD'.

The workplan of GOAHEAD includes 12 days of DNW-LLF wind tunnel tests (with the core model) in order to get a database for MR/TR CFD validation.

## 6. Conclusions

The versatility, adaptability, flexibility, and usefulness of the full helicopter wind tunnel model was demonstrated.

The unique combination of fuselage, Mach-scaled main rotor, and tail rotor allows to validate even sophisticated codes.

The possibility to trim the wind tunnel model in roll, pitch and yaw is a prerequisite to simulate free-flight conditions.

The model control software is a versatile tool to reach model trim within a few iteration steps, which improves considerably the efficiency, i.e. the ratio between data points and tunnel occupation time.

The broad band of sensor equipment and measurement technique allow to gain

- detailed flow field information
- unsteady local blade pressure at pre-defined blade locations
- steady state rotor hub loads, tail rotor loads, and fuselage loads
- local fuselage dynamic pressure
- flight test and wind tunnel data correlation concerning 3/rev and 4/rev hub and blade loads
- blade section position w.r.t. flap, lead-lag, and torsion

Moreover, parameter studies can simply be accomplished, since both - main rotor and tail rotor - use their own drive system.

## 7. References

[1] Langer, H.-J.; Junker, B.; Plassmeier, V.; Buchner, F.; Mikulla, V.; Mercker, E.:

The Unique Capabilities of a Complete Mach-Scaled Helicopter Model for the DNW-LLF. Paper #50, 27<sup>th</sup> European Rotorcraft Forum, Moscow, 2001

[2] S.G. Voutsinas, G. Arnaud, A. Dummel, D. Falchero, M. Pidd, J. Prospathopoulos, A. Visingardi, J. Yin: Aerodynamic Interference in Full Helicopter Configurations and Assessment of Noise Emission: Pre-test Modelling Activities for the HeliNOVI

Experimental Campaign; 31st European Rotorcraft Forum; FIRENZE, Italy; Sept 13-15, 2005

[3] O. Dieterich, A. Visingardi, H.-J. Langer, G. Imbert, M. Hounjet, S. Voutsinas, I. Cafarelli, R. Calvo, C. Clerc, K. Pengel: HeliNOVI - Current Vibration Research Activities; 31st European Rotorcraft Forum; FIRENZE, Italy; Sept. 13-15, 2005

[4] Yin, J., Berend Van der Wall, B., Oerlemans, S., et al: Representative Test results from HELINOVI Aeroacoustic Main Rotor/Tail Rotor/Fuselage Test in DNW; 31st European Rotorcraft Forum; FIRENZE, Italy; Sept. 13-15, 2005

[5] K. Pengel, R. Müller, B.G.van der Wall, Stereo Pattern Recognition – the Technique for Reliable Rotor Blade Deformation and Twist Measurements, AHS International Meeting on Advanced Rotorcraft Technology and Life Saving Activities, Utsunomiya, Tochigi, Japan, 2002

[6] O. Schneider, B.G. van der Wall, Final Analysis of HART II Blade Deflection Measurement, 29<sup>th</sup> European Rotorcraft Forum, Friedrichshafen, Germany, 2003

[7] Boer, J.F.; Hermans, C.; Pengel, K.: Helicopter Ground Vortex Comparison of Numerical Predictions with Wind Tunnel Measurement. Paper #25, 27<sup>th</sup> European Rotorcraft Forum, Moscow, 2001

[8] H.-J. Langer, R.L.Peterson, T.H.Meier: An Experimental Evaluation of Wind Tunnel Wall Correction Methods for Helicopter Performance; AHS 52nd Annual Forum, Washington, D.C., June 4-6, 1996.

[9] J.T. Heineck, G.K. Yamauchi, A.J. Woodcock, L. Laurenco: Application of Three-Component PIV to a Hovering Rotor Wake, 56th Annual Forum of the American Helicopter Society, Virginia Beach, VA, USA, 2000

[10] B.G. van der Wall, H. Richard: Analysis Methodology for 3C PIV Data, 31st European Rotorcraft Forum, Florence, Italy, 2005

[11] P.B. Martin, J.G. Pugliese, J.G. Leishman, S.L. Anderson: Stereo PIV Measurements in the Wake of a Hovering Rotor, 56th Annual Forum of the American Helicopter Society, Virginia Beach, VA, USA, 2000

[12] B.G. van der Wall, C.L. Burley, Y.H Yu, H. Richard, K. Pengel, P. Beaumier: The HART-II

test - measurement of helicopter rotor wakes, Aerospace Science and Technology, Vol. 8, pp. 273-284, 2004

### Author's Contact Addresses

Author:

juergen.langer@dlr.de

Co-authors:

Vibration: oliver.dieterich@eurocopter.com

Acoustic Array: stefan@nlr.nl (S.Oerlemans)

SPR: oliver.schneider@dlr.de

PIV: berend.wall@dlr.de

Acoustics: jianping.yin@dlr.de

### Appendix

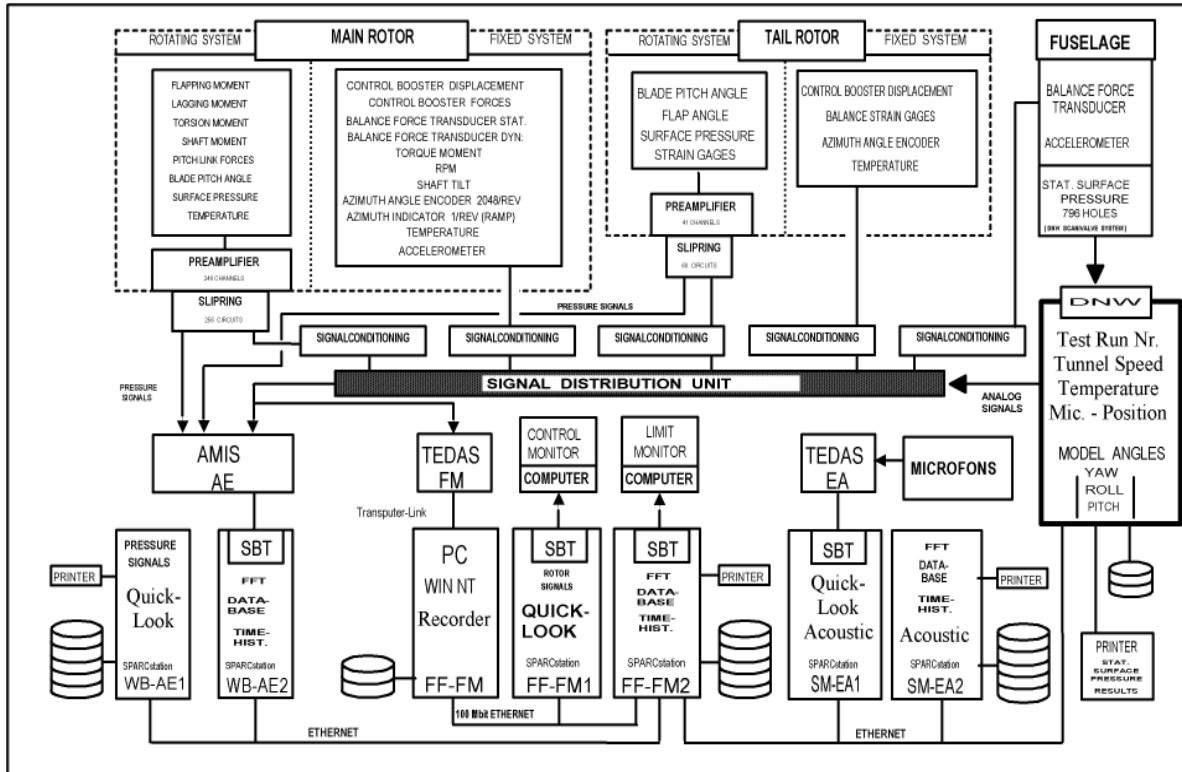


Figure 26: Signal flow chart

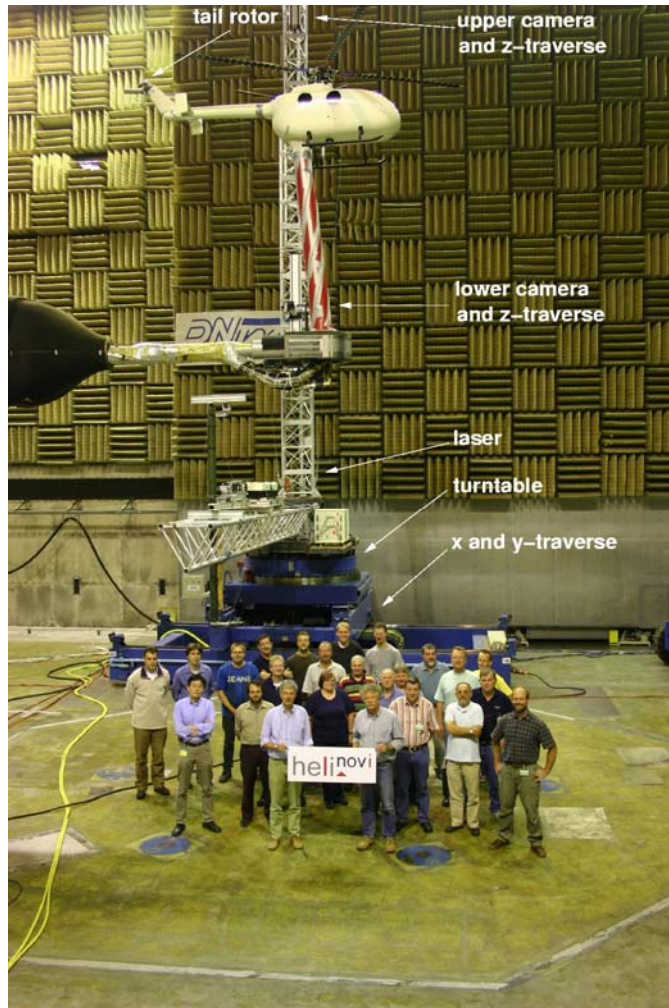


Figure 27: Test set-up for PIV measurements

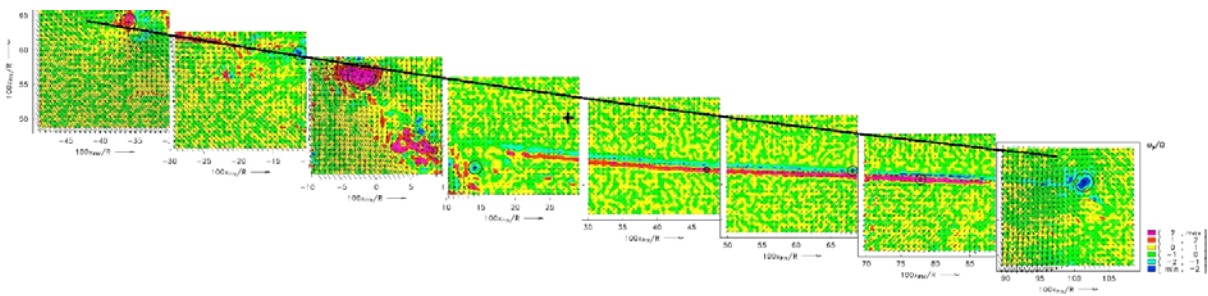


Figure 28: Flow field and vorticity distribution in a plane on the retreating side of the main rotor ( $y/R = -0.721$ ),  $V = 12$  m/s,  $\alpha = 8.1^\circ$ ,  $\Psi = 45^\circ$ .

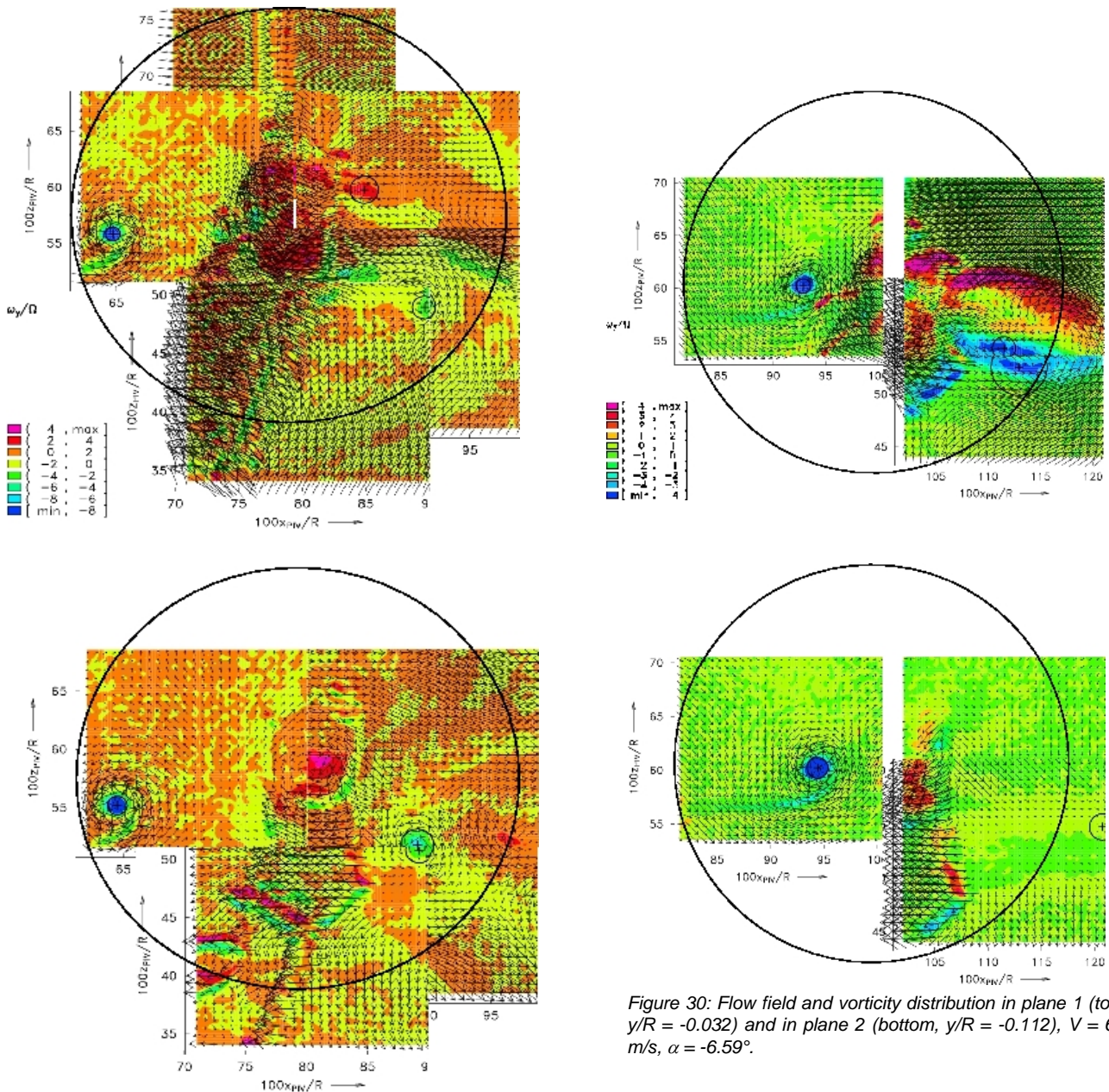


Figure 29: Flow field and vorticity distribution in plane 1 (top,  $y/R = -0.032$ ) and in plane 2 (bottom,  $y/R = -0.112$ ),  $V = 33$  m/s,  $\alpha = -13.5^\circ$ .

Figure 30: Flow field and vorticity distribution in plane 1 (top,  $y/R = -0.032$ ) and in plane 2 (bottom,  $y/R = -0.112$ ),  $V = 60$  m/s,  $\alpha = -6.59^\circ$ .